Macromolecular Materials and Engineering

Macromolecular Materials and Engineering Open Access
www.mame-journal.de

RESEARCH ARTICLE OPEN ACCESS

Interfacial Energy and Composition Controlled Self-Stratification in Polyurethane Coatings

Gaurav Singhal[1] | Lihong Lao[1] | Michaeleen L. Pacholski[2] | Harshad Shah[3] | Junsi Gu[2] | Bryan Caruso[2] | Fabio Aguirre-Vargas[3] | Piyush Singh[1] | Kshitish A. Patankar[2] | Simon A. Rogers[4] | Charles M. Schroeder[5] | Paul V. Braun[5]

[1]Materials Research Laboratory, Department of Materials Science and Engineering, Beckman Institute for Advanced Science and Technology, University of Illinois Urbana-Champaign, Urbana, IL, USA | [2]The Dow Chemical Company, Collegeville, PA, USA | [3]The Dow Chemical Company, Lake Jackson, TX, USA | [4]Department of Chemistry, Department of Chemical and Biomolecular Engineering, University of Illinois Urbana-Champaign, Urbana, IL, USA | [5]Materials Research Laboratory, Department of Material Science and Engineering, Department of Chemistry, Department of Chemical and Biomolecular Engineering, Beckman Institute for Advanced Science and Technology, University of Illinois Urbana-Champaign, Urbana, IL, USA

Correspondence: Paul V. Braun (pbraun@illinois.edu)

Received: 3 November 2025 | **Accepted:** 6 November 2025

Keywords: coatings | hydrophilic | hydrophobic | polyurethane | self-stratifying

ABSTRACT

Self-stratifying polymer systems are of great interest for coatings, as such systems reduce the time, cost, and environmental impact associated with the application of multilayered coatings by providing several layers in a single coating step. We have developed an understanding of self-stratification in polyurethane systems that occurs when hydrophobic and hydrophilic polyols containing ethylene oxide, propylene oxide, and butylene oxide mers and prepolymers containing toluene diisocyanate and methylene diphenyl diisocyanate are mixed and cured. When these components are mixed in appropriate proportions, self-stratification occurs where the hydrophobic component migrates to the air interface and the hydrophilic component to the substrate interface, with a thin hydrophobic layer present at the substrate walls when the substrate is hydrophobic. Self-stratification requires less than 60 min, significantly less than the time required for the storage modulus to crossover the loss modulus (~5 h). SIMS, XPS, and confocal Raman show that the stratification process at the air and substrate interfaces is dependent on interfacial surface energies, with the thickness and composition of the up to 10 μm thick interfacial region at the substrate controlled by the substrate surface energy. Self-stratification is observed in both the bulk and thicknesses conventionally associated with coatings (10s of μm).

1 | Introduction

There is a constant pursuit for coatings solutions that combine exceptional performance at an acceptable cost with reduced environmental impact. Self-stratifying coatings (SSCs), coatings that spontaneously separate into distinct layers during curing, in particular have garnered significant attention [1–4]. The primary interest in SSCs is that they enable the replacement of multiple coating steps with a single coating step, making possible cost reductions and performance enhancements [5–8]. In contrast, current coating systems generally consist of multiple layers, each serving a specific purpose, such as adhesion promotion [9, 10], barrier protection [11], or UV resistance [12–14], with each layer applied separately in steps that are time-consuming, labor and energy-intensive, and prone to introducing defects [15, 16].

SSCs rely on carefully designed chemical formulations that undergo phase separation during curing [17], where phase separation results in the formation of distinct layers, each exhibiting unique properties and functionalities [18, 19]. Stratification

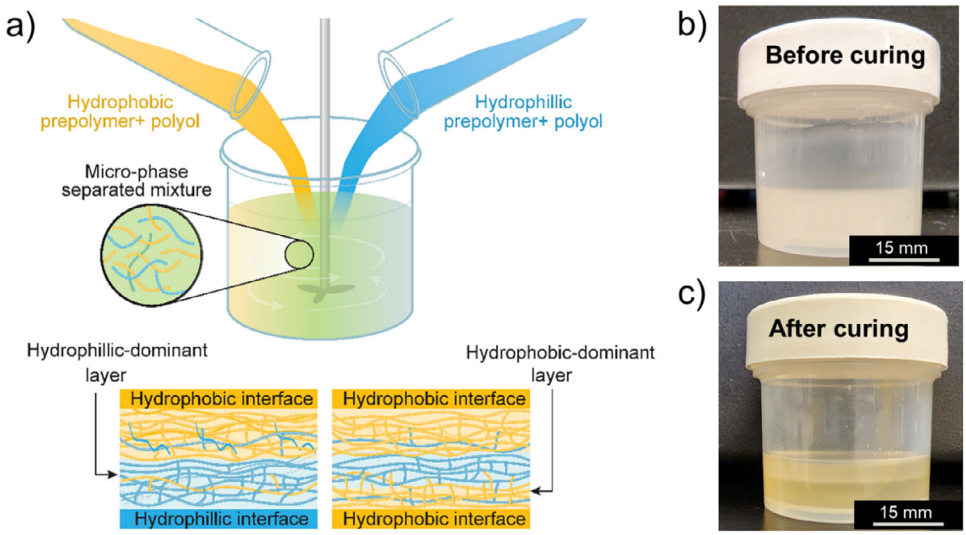

FIGURE 1 | (a) Illustrative schematic of the SSC. The same SSC stratifies into two layers when there is a hydrophobic interface at the top and a hydrophilic interface at the bottom and three layers when both the top and bottom interfaces are hydrophobic (the system-air interface is considered to be hydrophobic), (b) Optical image of the coating system immediately after mixing, (c) Optical image of the same sample after curing at 50°C for 24 h under vacuum.

involves a delicate balance between polymer chemistry, curing conditions, and the interaction of various components within the coating system [20, 21], making it a ripe area for scientific investigation. SSCs generally consist of chemistries that separate spontaneously into two continuous layers to form a layered coating [6, 22, 23], although, as we find here, more than two layers can form. One particular application of SSCs are where layering improves adhesion to the substrate.[24, 25] One set of example systems consists of mixtures of powdered polymers applied on a metallic substrate, where heating the polymers triggers layering which minimizes interfacial energies [26–28]. Solvent-based and waterborne SSC systems have also been studied [29–31].

Polyurethane coatings have long been valued for their excellent mechanical properties [9], chemical resistance [32–34], and thermal applications [35–39]. However, the study of polyurethane SSC systems has been limited. One study reported migration of single functionalized chains in a polyurethane blend, which shows inconsistent surface segregation [40]. Other studies reported core–shell like polyurethane/polyurea structures self-stratifying at the oil-water interface due to hydrophobic/hydrophilic interactions [11, 41] and the surface energy dependence of components in polyurethane systems leading to self-stratification [4]. The effect of crosslinkers on the degree of stratification of polyurethanes has also been investigated [1, 4]. An analysis of the kinetics, diffusion dynamics, and thermodynamics of such systems has not been reported. Here, we investigate the science of the stratification process in polyurethanes to provide the underpinnings necessary to optimize and design such systems.

We specifically examine an SSC polyurethane system containing hydrophilic and hydrophobic polyols, and hydrophilic and hydrophobic prepolymers (Figure 1). The hydrophilicity of these components is mainly due to the primary, secondary, and tertiary carbon/OH content. We find that how these components arrange themselves is primarily influenced by their surface properties, not their density or rheological properties. When this system cures, it naturally separates into hydrophobic and hydrophilic layers. From a practical standpoint, the fact that the system separates into distinct hydrophobic and hydrophilic layers is useful. The hydrophilic part wets and adheres to hydrophilic substrates, while the hydrophobic part prolongs the coating's lifespan. We note, we find that the two-layered coating converts to a three-layered coating when the substrate is hydrophobic. To understand the self-stratification process, the coatings are investigated using Secondary Ion Mass Spectrometry (SIMS), X-ray Photoelectron Spectroscopy (XPS), and confocal Raman spectroscopy, and the cure kinetics are monitored via DSC. The relationship of cure kinetics, rheology, and stratification is elucidated.

2 | Results and Discussion

2.1 | Characterization of Polyurethane Precursors

Materials for this study, including hydrophobic and hydrophilic prepolymers and polyols, were supplied by The Dow Chemical Company. Characterization was conducted to elucidate the chemical and physical factors relevant to stratification and the chemical factors contributing to the hydrophilic and hydrophobic properties of these components.

2.1.1 | Chemical Characterization Via Raman Spectroscopy and SIMS

SIMS (Figure 2b) identified TDI and MDI as the isocyanates present in prepolymers (see Section 2.3 for details). Raman spectroscopy (Figure S1) of the components revealed distinct differences between the hydrophobic and hydrophilic prepolymers and polyols. The hydrophobic prepolymer, formulated with MDI as the isocyanate, exhibited a pronounced shoulder peak at approximately 2950 cm^{-1} (Figure S1b), corresponding to the methyl ($-CH_3$) stretch. This peak indicates a higher concentration

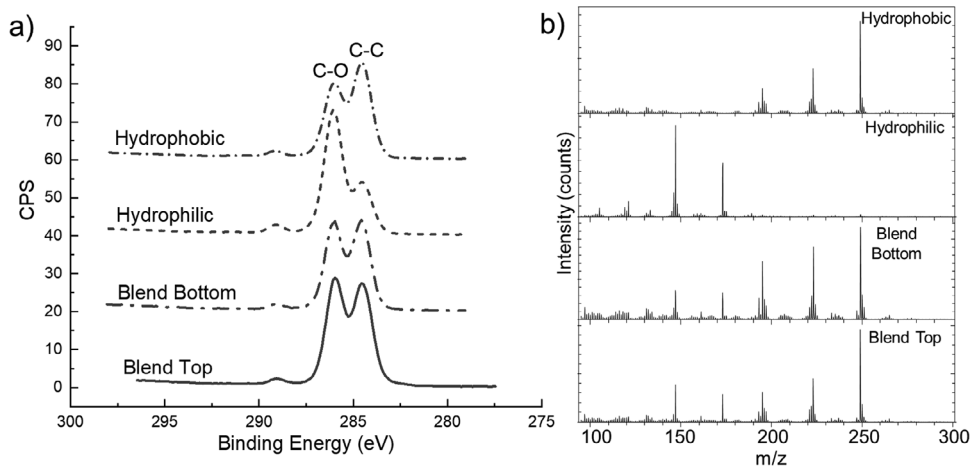

FIGURE 2 | (a) C1s XPS spectra of hydrophobic and hydrophilic films cured separately, along with a scan of the sample in Figure 1c once removed from the curing jar. There is a distinct difference in the C1s peak from the hydrophobic and hydrophilic films. Scans taken at the top and bottom surfaces appear similar (b) SIMS surface spectra of hydrophobic film and hydrophilic film cured separately (without mixing the hydrophilic and hydrophobic components), along with a spectrum of the sample in Figure 1c once removed from the curing jar. SIMS spectra taken at the top and bottom surfaces. SIMS spectra are normalized to the most intense peak in this mass range.

of secondary and/or tertiary carbon atoms within the polymer branches, which contribute to its hydrophobic character. A similar spectral feature was observed in the hydrophobic polyols, further reinforcing the relationship between structural branching and hydrophobicity. Additionally, the Raman spectrum for hydrophilic prepolymers and polyols displayed peaks primarily associated with ethylene oxide (EO), as shown in Figure S1a [42, 43].

Conversely, hydrophilic prepolymers containing TDI exhibited a significantly lower intensity of the methyl ($-CH_3$) peak. This attenuation indicates a higher proportion of primary and secondary carbons in the branches of the hydrophilic polyols, which align with their reduced hydrophobic character. This difference in carbon branching corroborates established theories that tertiary carbons are more hydrophobic compared to primary and secondary carbons due to their reduced polarity and limited ability to form hydrogen bonds [44, 45].

2.1.2 | Correlation Between Carbon Branching and Hydrophobicity

It is well-documented that hydrophobicity is heavily influenced by the molecular structure, particularly the ratio of primary, secondary, and tertiary carbons in hydrocarbon chains [44, 45]. Tertiary carbons, due to steric effects and electron-donating alkyl groups, exhibit significantly lower hydrophilicity compared to their primary and secondary counterparts. These findings are consistent with the observed spectral data (Table 1) and provide a chemical basis for the hydrophobic and hydrophilic characteristics of the materials studied.

2.1.3 | Thermal Properties

Differential scanning calorimetry (DSC) was employed to evaluate the glass transition temperatures (T_g) of the cured films. T_g of hydrophobic films was markedly higher than that of their hydrophilic counterparts, likely due to the rigid molecular structure imparted by the MDI-based prepolymers and their extensive secondary and tertiary branching (Table 1). Hydrophilic films, in contrast, exhibited lower T_g values, which can be attributed to the presence of TDI and the higher flexibility of primary and secondary carbon chains. The thermal properties are summarized in Table 1.

2.2 | Stratification Into 2- and 3-Layered Polyurethane System

In Figure 1, we illustrate the SSC before and after cure. The initial step is to create mixtures of hydrophilic prepolymer and polyol and hydrophobic prepolymer and polyol. These mixtures are combined in a stoichiometric ratio (refer to section 4.1), resulting in a microphase-separated system (Figure 1b). Upon cure, this mixture stratifies, forming at least two distinct layers (optical image in Figure 1c). As detailed in the following sections, the stratification process is highly dependent on the interface surface energy, operates in both bulk and thin film, and can yield more than two layers when the substrate is hydrophobic, as illustrated in Figure 1a.

2.3 | Surface Analysis Via XPS and SIMS

Upon analyzing the cured sample's surfaces (cured in a hydrophobic container), we observe that the top and bottom surfaces of the blended sample appear remarkably chemically similar. XPS (Figure 2a) reveals C-O and C-C peaks [46], stemming from the polyol and prepolymer backbone, with the data suggesting the surfaces consist primarily of hydrophobic polymer (higher primary carbon content) with some hydrophilic polymer present (the C-O to C-C ratio at the top and bottom surfaces more closely resembles the hydrophobic polymer than the hydrophilic polymer). SIMS (Figure 2b) shows the atomic mass on *x*-axis

TABLE 1 | Qualitative analysis of the prepolymers and polyols.

Component	Isocyanate	Oxide	Key Raman Features	T_g for cured films (°C)	Viscosity at 22°C (cps)
Hydrophilic Prepolymer	TDI	EO	• Weak CH_3 stretch at 2950 cm^{-1} • TDI peak in SIMS spectra	~-25	21400
Hydrophilic Polyol		EO	• Weak CH_3 stretch at 2950 cm^{-1}		200
Hydrophobic Prepolymer	MDI	PO/BO	• Pronounced CH_3 stretch at 2950 cm^{-1} • MDI peak in SIMS spectra	~9	570
Hydrophobic Polyol		PO/BO	• Pronounced CH_3 stretch at 2950 cm^{-1}		350

and agrees with this assessment as peaks specific to both the hydrophobic (MDI, 250 g/mol) and hydrophilic (TDI, 174 g/mol) polymers are present at the top and bottom surfaces, with peaks associated with the hydrophobic polymer being enhanced relative to those associated with the hydrophilic polymer. While optical images show the formation of two distinct layers post-curing, XPS and SIMS indicate at least three layers are present. It is noted that the difference in the counts in the SIMS measurement cannot be directly related to the concentration of the components due to the difference in ion yield during measurement. To further evaluate the structure, we conducted analyses using confocal Raman microscopy.

2.4 | Cross-Section Profile with Raman Microscopy

Confocal Raman microscopy on the cured hydrophilic and hydrophobic polymers shows a substantial contrast in the CH_3 stretching intensities between the two (Figure 3a). As seen in the Raman scans of the components (Figure S1), the CH_3 stretching intensities stem from hydrophobic prepolymers and polyols. Notably, the hydrophobic coating exhibits a stronger Raman intensity at 2950 cm^{-1}, corresponding to the CH_3 stretching peak [47], consistent with the XPS results. This peak serves as a marker for distinguishing between the hydrophilic and hydrophobic components in our subsequent confocal Raman scans. To facilitate this analysis, we prepared a flat cross-section of a cured blend film through microtomy, as depicted in Figure 3c. The Raman spectra collected at the cross-section and at equidistant points from the surface and the interface, as described in the Figure 3 caption, reveal that the marker peak intensity remains consistent at the surface and within the top layer (points i, ii, iii). However, upon crossing the interface, the peak intensity diminishes, confirming the bottom layer is more hydrophilic. The points within the cross-section of the bottom layer display similar CH_3 content in Raman measurements as expected. Notably, the CH_3 peak intensity increases once again when measuring the bottom surface, further evidence that what initially appears to be a two-layer stratification is, in fact, a sandwich structure consisting of a hydrophilic-dominant layer sandwiched between a thicker (at the top) and a thinner (at the bottom) hydrophobic layer. The polymer blend was cured within a polypropylene container in a vacuum oven, and thus both the interface with the container and the vacuum are hydrophobic in character. This suggests the formation of the thin hydrophobic layer at the bottom is driven by surface energy.

2.5 | Effects of Substrate Hydrophobicity on Stratification

To investigate the effect of substrate surface energy, the blend is cured between two hydrophilic surfaces and between hydrophilic and hydrophobic surfaces, with the hydrophilic substrates in the first case consisting of gold-coated wafers functionalized with sodium 3-mercapto-1-propanesulfonate [48], and the hydrophilic substrate in the second case consisting of a clean glass slide functionalized with a hydroxyl group using piranha treatment. Depth profiling is performed using SIMS, leveraging the TDI signature in hydrophilic and the MDI signature in hydrophobic films mentioned in Figure 2b as markers to differentiate the components. The film sandwiched between two hydrophilic silicon substrates (total thickness ~50 μm) contains thin hydrophilic layers at both interfaces separated by a thick hydrophobic layer, as identified by a sharp initial decrease in the hydrophilic functional group concentration (TDI) and sudden increase near the polymer film-substrate interface (Figure 4a). The SIMS spectra for the blend spun-coat on a hydrophilic glass slide (~30 μm thick) show two distinct hydrophobic and hydrophilic layers (Figure 4b) at the respective interfaces. We note the coatings remain self-stratifying when thin, as important for most coating applications.

In SSCs polymer blends, enthalpic and entropic effects on behavior at interfaces are important to consider [49–52]. Enthalpic contributions arise from the interactions of different components of the polymer blend with the material comprising the interface. Entropic effects, which can also determine which components of a polymer blend segregate to an interface, are influenced by factors such as molecular weight, chain stiffness, and polymer architecture [53, 54], factors which determine the degree of reduction in polymer configurational entropy near an interface. In the specific SSC system investigated here, the similarity in molecular weight, architecture, and end groups of the hydrophilic and hydrophobic polymers (Table 1) reduces the impact of entropic contributions, and enthalpic effects probably dominate. As such, we suggest the primary driving force for film formation at the interfaces investigated here is the difference in surface energy between the hydrophilic and hydrophobic polymers. Using the pendant drop technique, the surface energy of the hydrophobic polymer is measured to be 32 N/mm and the hydrophilic polymer 45 N/mm (Figure S6). This difference in surface energy serves as the primary driving force for one polymer or the other to create a stable film at the polymer-substrate interface. When the interface is relatively hydrophobic (γ < 35 mN/m) the

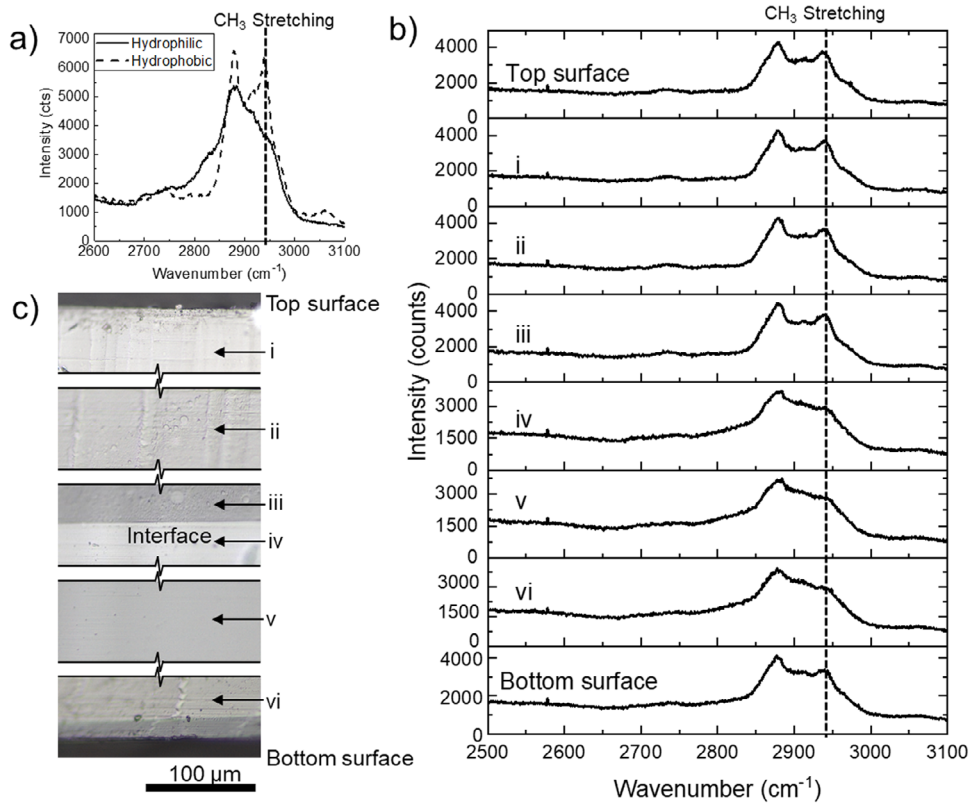

FIGURE 3 | (a) Confocal Raman spectra of hydrophobic film and hydrophilic polymers cured separately. (b) Confocal Raman spectra of regions of a cross-section of the sample shown in Figure 1c. (c) Optical microscope image of the sample scanned in b) showing the locations of the scans. Points i and vi are ~50 µm below/above the top/bottom surfaces. Points ii and v are about midway between the surfaces and the interface at the sample center, and points iii and iv are ~20 µm either side of the center interface.

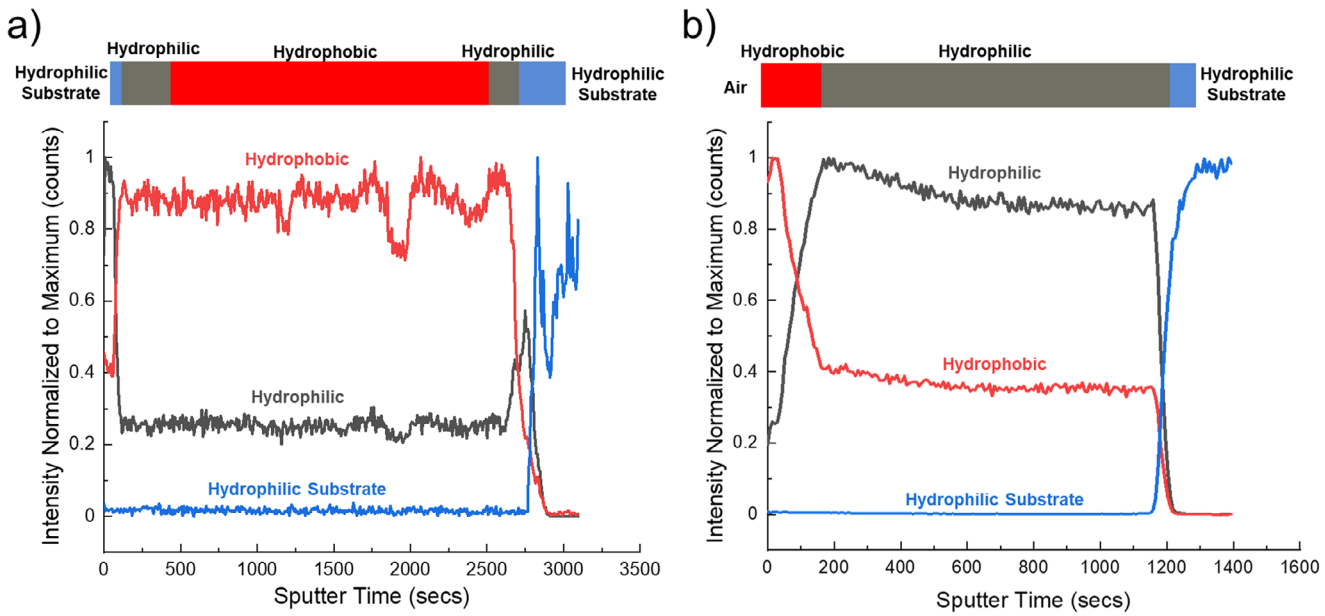

FIGURE 4 | (a) SIMS depth profile from a ~50 µm thick polyurethane blend sample cured between two hydrophilic substrates showing 3-layered stratification. Note, the top hydrophilic substrate is removed prior to SIMS analysis. (b) SIMS depth profile from a polyurethane blend cured on a hydrophilic substrate with the other interface being vacuum, indicating 2-layered stratification with hydrophobic content at the top.

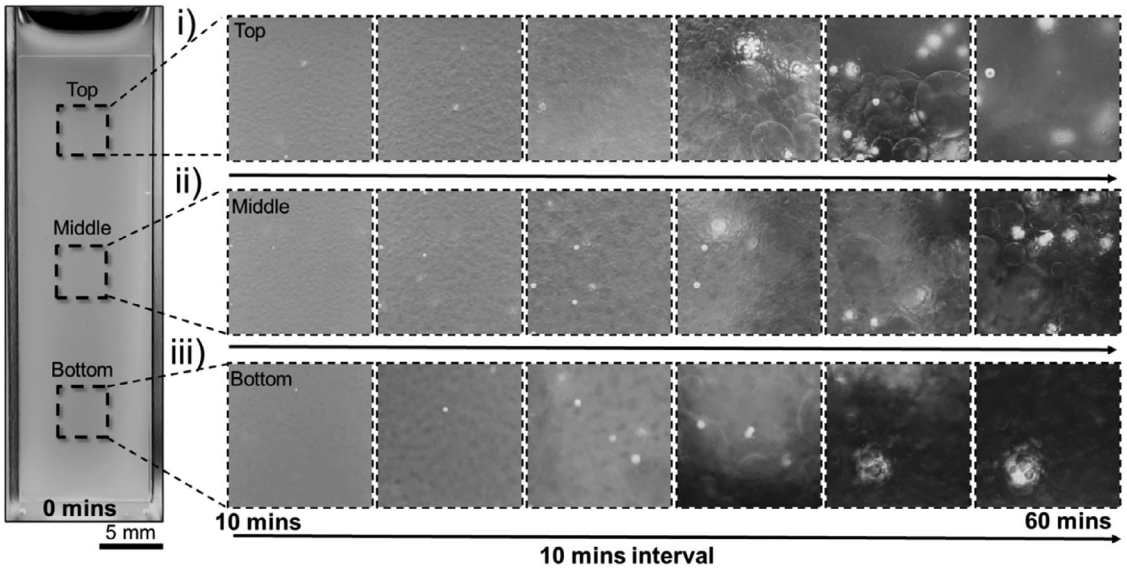

FIGURE 5 | Optical image of PU blend sample cured inside a plastic cuvette. (i) Optical image of the sample at the top region, picture taken every 10 mins, left to right. (ii) Optical image of the sample at the middle region, picture taken every 10 mins, left to right. (iii) Optical image of the sample at the bottom region, picture taken every 10 mins, left to right.

hydrophobic components ($\gamma \sim 32$ mN/m) migrate to the interface, whereas, when the interface is relatively hydrophilic ($\gamma > 45$ mN/m) the hydrophilic components ($\gamma \sim 45$ mN/m) migrate to the interface.

2.6 | Optical Imaging of Stratification Over Time

Optical imaging of the phase separation (Figure 5) helped identify the phase separation/stratification mechanism. The microphase-separated mix right after blending undergoes a coalescence process where initially the microphase-separated components form larger droplets. After about 30 min, the stratified layers start forming. After about 1 h, the top and bottom layers are formed with some droplets trapped within the layers. The center of the sample remains more mixed phase with droplets remaining in a matrix.

2.7 | Effect of Mixing Ratios on Stratification

The relationship between mixing ratios (hydrophilic: hydrophobic) and phase separation is investigated across ratios of 4:1, 2:1, 1:1, 1:2, and 1:4 using scanning electron microscopy (SEM) and confocal Raman spectroscopy (Figure 6). The findings revealed stratification occurring at ratios of 2:1 and 1:1, while the remaining ratios displayed microphase separation with droplet-like structures composed primarily of either hydrophobic or hydrophilic components (Figure 6a–e). Not surprisingly, the component in excess became the matrix, while the minority component contributed to droplet formation, supported by Raman data (Figure 6f) indicating hydrophobic interiors in ratios with higher hydrophilic content. However, in the 1:2 and 1:4 ratios, both inside and outside the droplets exhibited hydrophobic components, potentially due to the small droplets being below the sampling volume of the confocal Raman microscope, though distinct phases are seen inside and outside the droplets in the SEM images. Reanalysis using secondary ion mass spectrometry (SIMS) validated these findings (Figure 7).

SIMS images (Figure 7) are presented for the samples shown in Figure 6d (hydrophilic:hydrophobic ratio 1:2) and Figure 6a (hydrophilic:hydrophobic ratio 4:1). SIMS images show mixed regions of hydrophobic and hydrophilic functional groups with droplets like microstructures. The 1:2 ratio shows droplets of hydrophilic functional group distributed in the matrix of hydrophobic functional group, confirming that the component present in excess (hydrophobic) forms the matrix while the lesser component forms the droplets (Figure 7a). The reverse trend is observed for the mixing ratio of 4:1 (Figure 7b).

2.8 | Rheology Evolution During the Stratification Process

Complex viscosity is determined by analyzing the loss modulus (G″) and storage modulus (G′) of hydrophilic and hydrophobic mixtures. Loss modulus (G″) is a measure of the energy dissipated within a material during deformation, reflecting its viscous behavior. In contrast, storage modulus (G′) represents the energy stored within a material and reflects its elastic characteristics. The observation that the magnitude of complex viscosity of the hydrophobic mixture surpasses the hydrophilic mixture around 25 min after the initial blending of prepolymers and polyols indicates an earlier shift from predominantly viscous to more elastic behavior in the hydrophobic mixture (Figure 8a). The initially high viscosity of the hydrophilic mixture can be attributed to the significantly higher viscosity of its prepolymer component (Table 1). The first peak observed in the storage modulus of the hydrophobic mixture (Figure 8b) might be indicative of loss of mobility which is around 40 min, this peak is followed by an energy dissipation period during which most of the curing takes place, followed by another peak which indicates near complete gelation. Furthermore, the transition of both storage and loss

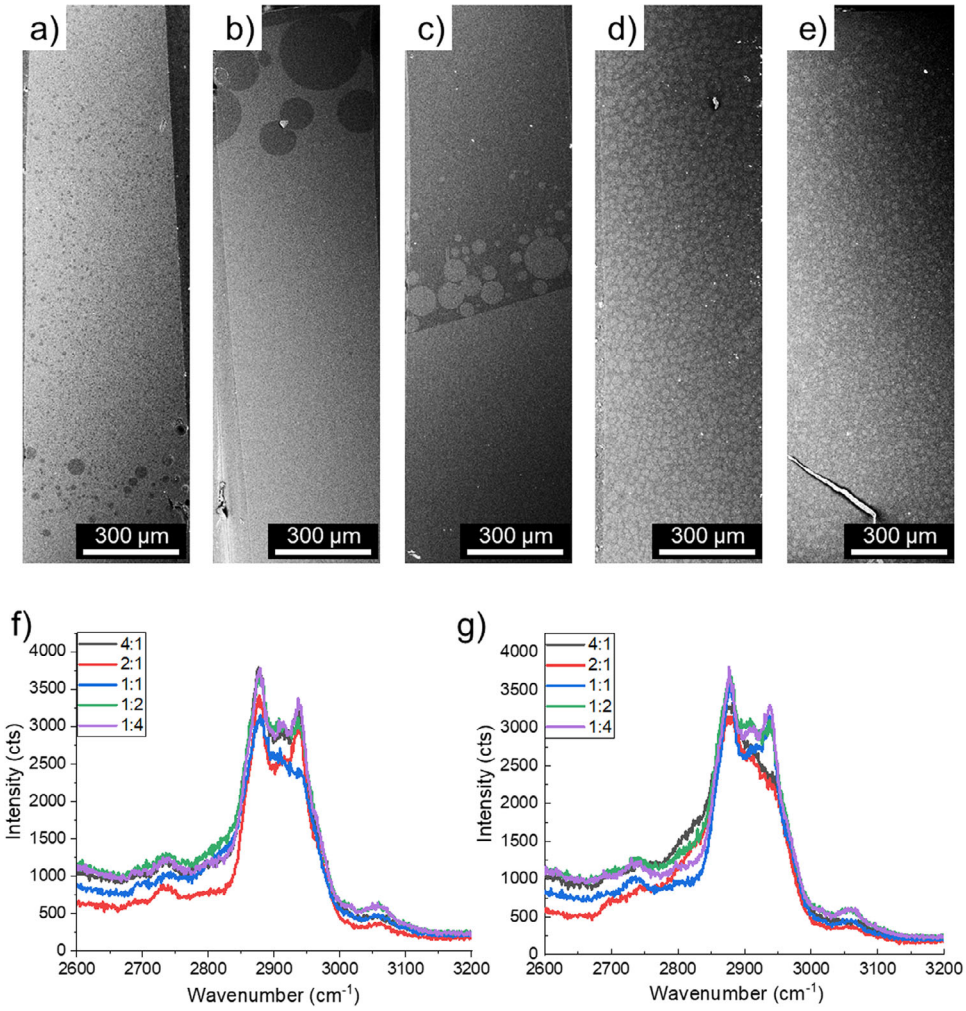

FIGURE 6 | Cross-sectional SEM of cured films of PU blends with a hydrophilic to hydrophobic blend ratio of (a) 4:1, (b) 2:1, (c) 1:1, (d) 1:2, and (e) 1:4. (f) Confocal Raman spectra inside droplets for the indicated mixing ratios, (g) Confocal Raman spectra outside the droplets for the indicated mixing ratios.

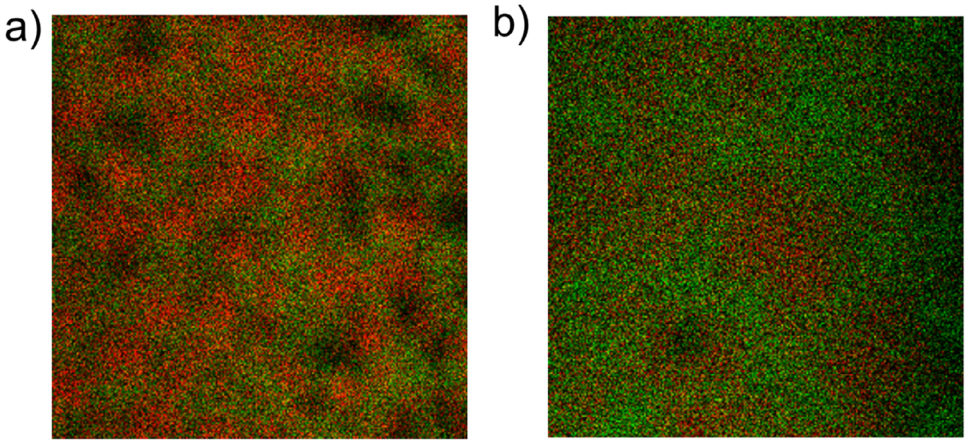

FIGURE 7 | Hydrophilic functional group (red) and hydrophobic functional group (green) SIMS images of the cross section of samples with mixing ratios (a) 1:2 (201 x 201 µm2), (b) 4:1 (135 x 135 µm2).

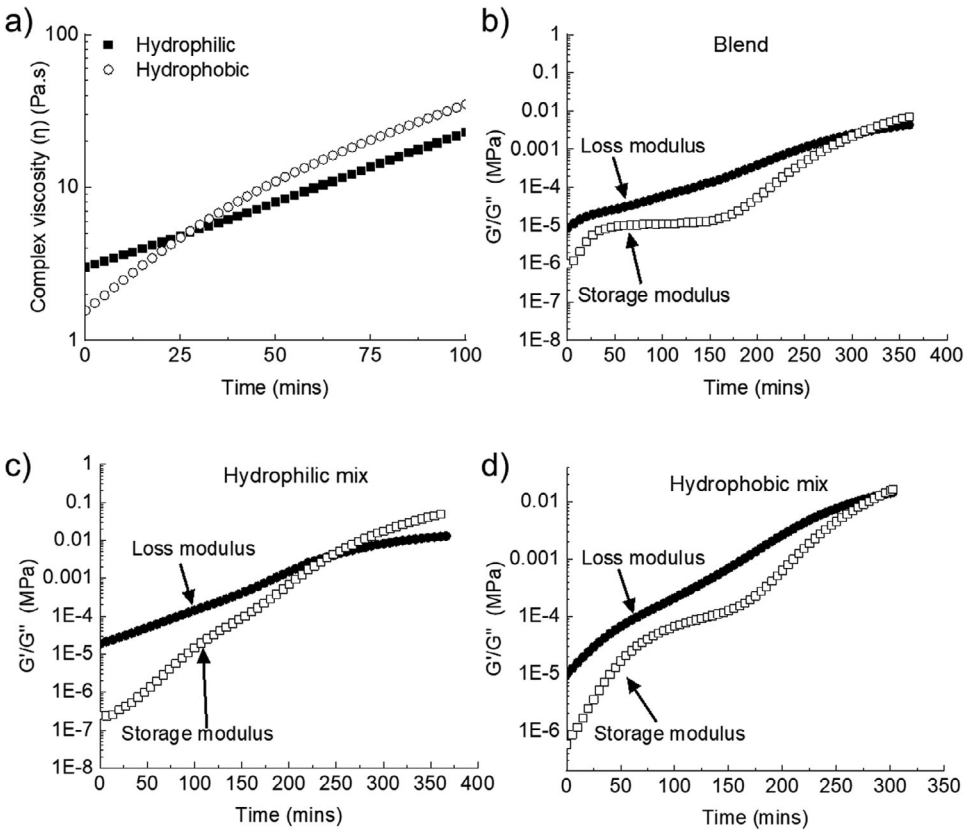

FIGURE 8 | Rheology data for the hydrophilic, hydrophobic, and blend mixes (ratio 1:1) (a) Magnitude of complex viscosity showing that crossover happens at ~25 mins for hydrophilic and hydrophobic films. (b) Storage modulus and loss modulus were measured for the blend showing crossover at ~ 300 mins. (c) Storage modulus and loss modulus measured for the hydrophilic mix showing crossover at ~ 250 mins. (d) Storage modulus and loss modulus measured for the hydrophobic mixture showing crossover at ~ 300 mins.

modulus from viscoelastic to an elastic state takes more than 3 h (Figure 8b–d), underscoring the time-dependent nature of the material's behavior. These observations, combined with imaging and other data, suggest that within the first hour after mixing, the system, regardless of the mixing ratios, loses its mobility, indicating that the loss modulus plays a pivotal role in driving the migration of components in the mixed state, a topic that will be further explored in the following paragraphs.

Reaction kinetics are measured using differential scanning calorimetry (DSC). The reaction rates are calculated from the degree of cure using the Arrhenius model as shown below [55].

$$\frac{d\alpha}{dt} = k[(1 - x_{sol})(1 - \alpha)]^m \quad (1)$$

where, α is the degree of curing, k is the reaction rate constant, m is the order of reaction, x_{sol} is mass fraction of non-reactive diluent (assumed zero here).

It has been observed that the hydrophobic prepolymer and polyol exhibit a relatively higher reaction rate compared to their hydrophilic counterparts (Figure 9a). When all four components are mixed together, the effective reaction rate constant is similar to a value that is the sum of the individual reaction rates of the hydrophobic and hydrophilic components. To investigate cross-reactions, DSC measurements were conducted on samples where hydrophilic prepolymer was mixed with hydrophobic polyol and vice versa, revealing negligible reaction rates in such cases. This allows us to confidently rule out the influence of cross-reactions. The DSC measurements also indicate the activation energies of these reaction systems align with typical values for the activation energy of urethane linkage formation (Figures S2–S5) [56], indicating external factors such as moisture or isocyanate-urethane reactions do not dominate the system response. The rheology data further indicate that the complex viscosity of the hydrophobic components surpasses that of the hydrophilic components within 25 min, likely due to the higher reaction rates of the former, as revealed by kinetic studies.

SSCs require bulk phase separation before the coating cures. Coalescence is one mechanism which can result in phase separation if sufficiently rapid relative to cure [57–59], In the polymer blend system here, coalescence is found to play a crucial role in the phase separation process during the curing of the coating. Images recorded during the phase separation process (Figure 5) show small droplets emerging over time, which eventually combine to form the stratified layer. Since there are no dynamic processes (like flow) taking place in the coatings here, coalescence can be termed as static and driven by factors like Brownian motion, van der Waals interactions, and sedimentation [37, 59].

As the viscosity increases, leading to a decrease in the Brownian motion, we observe a critical point during cure where

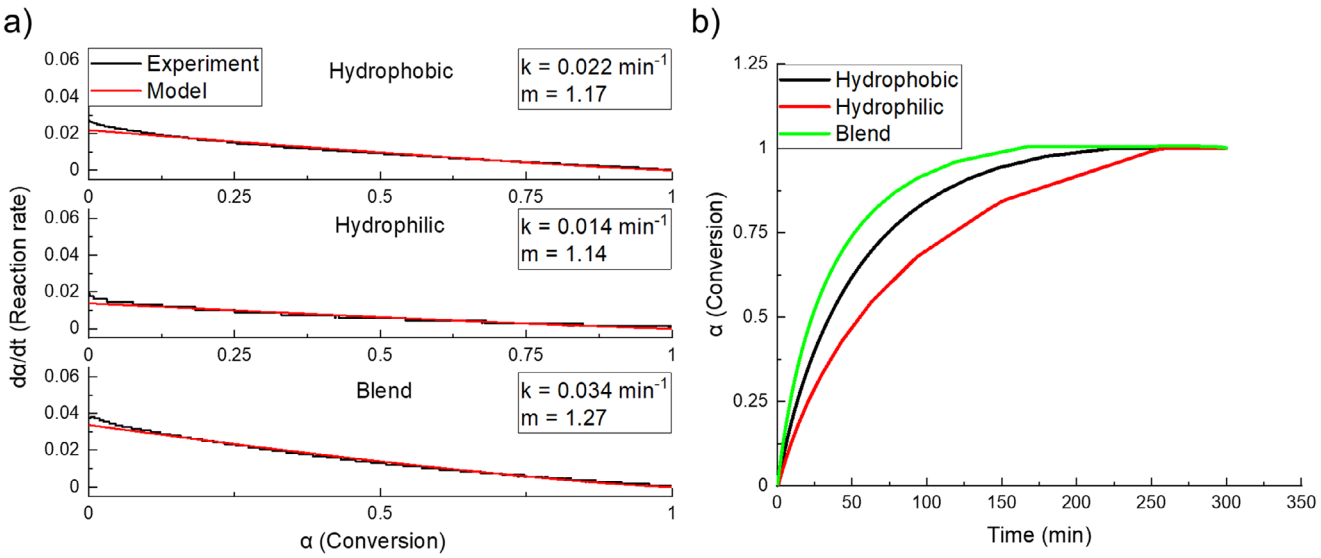

FIGURE 9 | Reaction kinetics calculated from the DSC data for hydrophobic, hydrophilic, and blend samples as they are reacting, (a) Reaction rates calculated from DSC data and fitted curves, with derived reaction constant k and order of reaction m, (b) Conversion plotted against time for hydrophobic, hydrophilic, and blend samples.

droplet growth is halted. Our rheology measurements indicate that the viscosity of hydrophobic components surpasses that of hydrophilic components in approximately 25 min. Consequently, we can infer that in systems with a higher proportion of hydrophobic components (specifically, ratios of 1:2 and 1:4) that exhibit faster reaction rates (as shown in Figure 9a), the growth of polymer droplets is impeded sooner compared to other ratios (4:1, 2:1, 1:1). In the latter ratios, where the hydrophilic components react more slowly, they provide sufficient time for the hydrophobic particles to grow and eventually coalesce.

3 | Conclusion

This research offers an understanding of the intricate interplay between interfacial energies and composition-driven phase separation morphologies in self-stratifying polyurethane systems. By employing XPS, SIMS, and confocal Raman spectroscopy, we have unraveled the mechanisms governing self-stratification, with a particular focus on the role of surface energies and bulk phase separation. These findings shed light on the forces at play during self-stratification, where components with specific surface energies tend to migrate and form stable films at the interface, a process operating in conjunction with the bulk phase separation process. The relationship between macroscopic phase separation and coalescence as viscosities change (as coupled to reaction rates) provides insights into when self-stratification can occur. The findings presented here are highly relevant to the design of Janus coating systems exhibiting contrasting hydrophilic and hydrophobic functionalities on opposing surfaces. By harnessing self-stratification driven by interfacial energy differences, such coatings can be fabricated in a single formulation, eliminating the need for sequential processing while achieving tailored interfacial and surface properties for applications such as corrosion protection, antifouling, and self-cleaning surfaces. The insights here will hopefully inform the optimization and design of tailored coatings for a diversity of purposes.

4 | Experimental Methods

4.1 | Sample Preparation

4.1.1 | Thick Films

The PU system under investigation comprises four key components: hydrophilic polyol, hydrophobic polyol, hydrophilic prepolymer, and hydrophobic prepolymer, all provided by Dow for the purpose of synthesizing polyurethane in bulk and film forms. For all samples analyzed, the hydrophilic film is composed of 74.6 wt.% hydrophilic prepolymer and 25.4 wt.% hydrophilic polyol, denoted as "hydrophilic mix." The hydrophobic film is composed of 56.4 wt.% hydrophobic prepolymer and 43.6 wt.% hydrophobic polyol, referred to as "hydrophobic mix." To create various ratios (4:1, 2:1, 1:1, 1:2, and 1:4), mixtures are prepared by combining different proportions of hydrophilic mix and hydrophobic mix. To ensure a thorough and uniform blend of the components, a speed mixer (FlackTek DAC 150.1 FVZ-K) is employed at 2400 rpm for 1 min each time a component is introduced. Once all components are thoroughly mixed, the materials are cured at 50°C in a vacuum oven. Following the curing process, a clear phase separation, as depicted in Figure 1c, becomes evident. Samples prepared as such were used for analysis shown in Figures 2, 3, 6, and 7.

Cross-sections were prepared using a cryo-microtome at −80°C. Microscopy analysis began with the Leica DM (digital microscope), where coaxial lighting and autoexposure settings were used to capture optical images of the samples.

4.1.2 | Thin Films

Functionalized glass slides and gold-coated silicon wafer were used as hydrophilic substrates. Hydrophilic glass slides were obtained by piranha cleaning the slides and treating them with

piranha acid, gold coated (100 nm Au e-beam evaporated) silicon wafers were functionalized with sodium 3-mercapto-1-propanesulfonate to make the surface hydrophilic. PU blend was spin coated on the hydrophilic glass slide at 2000 rpm for 60 sec and later cured in a vacuum oven at 50°C for 24 hrs. The PU blend was also sandwiched between the treated gold coated wafer with coverslip (50 microns thick) as a spacer and cured in a vacuum over at 50°C for 24 hr.

4.1.3 | XPS

Samples were analyzed using a Thermo Scientific K-Alpha X-ray photoelectron spectrometer with monochromatic Al Kα radiation. XPS data were acquired from four distinct areas across each sample to obtain representative elemental and chemical state information from the top 10 nm of the surface. The instrument parameters included a 90° take-off angle, 200 eV pass energy for survey spectra, and 20 eV pass energy for high-resolution spectra, with auto height enabled and a flood gun activated. Data were compared for all regions for consistency for each sample. The analysis software employed for data processing was Casa 2.3.17 Dev 6 3y.

4.1.4 | SIMS

Secondary ion mass spectrometry (SIMS) data were collected using an IONTOF V instrument with a 30kV Bi_3^+ primary ion source. For all data, charge compensation was used with approximately 2 μA of target current. For spectra of surfaces, data were collected in the bunched instrument modes over either 500 x 500 μm or 200 x 200 μm areas with 256 x 256 pixels in random raster mode for 20 scans with one shot per pixel. For images of cross sections, material that bloomed to the surface after sectioning needed to be removed using an Ar^+ gas cluster beam. For these images, an ~11 nA, 10kV Ar_{1200} sputter source was used in a noninterlaced sputter cycle with 10 sputter frames and a 2 s pause over a 500 x 500 μm area until the surface had visually sharper optical features and image contrast was seen in the data. At this point high quality images were acquired in the sputter crater at the 200 x 200 um field of view in the same manner as mentioned above. For the depth profiles shown in Figure 4, sputtering was accomplished using a 20 kVAr_{1500}^+ beam at ~16 nA with a 5 or 10 sputter cycle with a 1 sec pause in noninterlaced mode over a 500 x 500 μm area. Spectral data were acquired from regions of 128 x 128 or 256 x 256 pixels in random raster mode with 1 frame per sputter cycle with the conditions otherwise detailed above.

4.1.5 | Confocal Raman Microscopy

Raman microscopy was performed on a HORIBA LabRAM HR Raman microscope with a 50×, NA = 0.75 objective, employing a 785 nm laser (330 mW) with a user controllable variable aperture confocal pinhole (550 microns) that provides diffraction-limited spatial resolution with maximum signal throughput. The backscattered radiation was transmitted through a 50-μm diameter multimode fiber to a UHTS 300 spectrometer with a 300 groove mm^{-1} diffraction grating and back-illuminated CCD camera cooled to −65°C (Newton DU970 N−BV, Andor Technology Ltd. Belfast, UK). The incident laser power on the sample was measured to be 30 mW. Raman spectra were recorded at an integration time of 80 s. All the confocal Raman data presented in this manuscript is raw (without background subtraction and baseline adjustment).

4.1.6 | Scanning Electron Microscopy

Samples were prepared by cryo-microtomy (Leica UC7 cryo-microtome) at −80°C to form a flat face for SEM and SIMS imaging. SEM imaging was performed in the Hitachi 3400 SEM equipped with a W filament electron source operating at 10 kV. Images were captured under the low-pressure mode (40 Pa) with a back-scattered electron detector.

4.1.7 | Rheology

Rheology parameters were measured using a DHR-3 rheometer (TA Instruments). The samples were placed on the rheometer using parallel plate geometry with a disk diameter of 25 mm. Oscillation-amplitude measurements were first conducted with strain rate sweeping from 0.01% to 100% and frequency of 1 Hz at 60°C. After that, the oscillation-time measurements were conducted at the identified strain rate of 2% and frequency of 1 Hz at 60°C for up to 6 h, where the changes of storage modulus (G'), loss modulus (G''), and complex viscosity (η^*), along with the reaction, were recorded.

The viscosity of the prepolymer components at room temperature was found to be as follows: hydrophilic prepolymer: 21 400 cps, hydrophilic polyol: 200 cps, hydrophobic prepolymer: 570 cps, and hydrophobic polyol: 350 cps.(Table 1)

4.1.8 | DSC

DSC measurements were conducted using a TA Instruments DSC 2500. For these measurements, 5 to 10 mg samples were sealed in hermetic T_{zero} aluminum pans. Isothermal scans were collected for the hydrophilic, hydrophobic and blend samples to calculate the reaction constants and degree of cure. Normalized heat flow was also measured for hydrophilic, hydrophobic and blend samples by conducting ramp heating experiments at heating rates of 1°C, 2°C, 3°C, 4°C, 5°C, 6°C, 7°C, and 8°C min^{-1} in a temperature range of −40°C–250°C. All samples for DSC measurements were prepared in a glovebox in Argon atmosphere. Samples for isothermal and heat flow measurements were stored in a dry ice bath, after mixing the prepolymer and polyol and removed only when they were ready for DSC measurements.

Acknowledgements

The authors acknowledge the Dow University Partnership Initiative (UPI program) for financial support, and also the helpful discussions with Paul Mwasame (Dow), Decai Yu (Dow). The authors thank Hyeonmin Jeong

(UIUC) and Prof. Charles Sing (UIUC) for the insightful discussions. This research was carried out in part in the Materials Research Laboratory, University of Illinois at Urbana-Champaign and the input from staff scientists particularly Dr. Roddel Remy and Dr. Mohammad Amdad Ali is greatly appreciated.

Conflicts of Interest

The authors declare no conflict of interest.

Data Availability Statement

The data that support the findings of this study are available from the corresponding author upon reasonable request.

References

1. A. Beaugendre, S. Degoutin, S. Bellayer, et al., "Self-Stratifying Coatings: A Review," *Progress in Organic Coatings* 110 (2017): 210–241.

2. V. V. Verkholantsev, "Self-Stratifying Coatings for Industrial Applications," *Pigment & Resin Technology* 32 (2003): 300–306.

3. S. Benjamin, C. Carr, and D. Walbridge, "Self-Stratifying Coatings for Metallic Substrates," *Progress in Organic Coatings* 28 (1996): 197–207.

4. J. Baghdachi, H. Perez, P. Talapatcharoenkit, and B. Wang, "Design and Development of Self-Stratifying Systems as Sustainable Coatings," *Progress in Organic Coatings* 78 (2015): 464.

5. C. Ochoa, S. Gao, S. Srivastava, and V. Sharma, "Foam Film Stratification Studies Probe Intermicellar Interactions," *Proceedings of the National Academy of Sciences* 118 (2021): 2024805118.

6. T. J. Murdoch, B. Quienne, M. Argaiz, et al., "One Step Closer to Coatings Applications Utilizing Self-Stratification: Effect of Rheology Modifiers," *ACS Applied Polymer Materials* 5 (2023): 6672–6684.

7. S. Zahedi, D. Zaarei, and S. R. Ghaffarian, "Self-Stratifying Coatings: A Review," *Journal of Coatings Technology and Research* 15 (2018): 1–12.

8. D. Sharma and D. Mandal, "Self-Stratified Coating with Multiresponsive Self-Healing Polymer," *ACS Applied Polymer Materials* 5 (2023): 7051–7059.

9. H. Son, A. L. Chau, and C. S. Davis, "Polymer Thin Film Adhesion Utilizing the Transition from Surface Wrinkling to Delamination," *Soft Matter* 15 (2019): 6375–6382.

10. N. Deneke, A. L. Chau, and C. S. Davis, "Pressure Tunable Adhesion of Rough Elastomers," *Soft Matter* 17 (2021): 863–869.

11. P. K. Singh, M. L. Pacholski, J. Gu, et al., "Designing Multicomponent Polymer Colloids for Self-Stratifying Films," *Langmuir* 38 (2022): 11160–11170.

12. I. Babahan-Bircan, J. Thomas, and M. D. Soucek, "Environment-Friendly UV-curable Alkyd-Based Non-Isocyanate Urethanes," *Journal of Coatings Technology and Research* 19 (2022): 1507–1522.

13. Q. Wang, J. Thomas, and M. D. Soucek, "Investigation of UV-Curable Alkyd Coating Properties," *Journal Coatings Technology Research* 20 (2023): 545.

14. S. Kumar, M. Kumar, and N. Jindal, "Overview of Cold Spray Coatings Applications and Comparisons: A Critical Review," *World Journal of Engineering* 17 (2020): 27–51.

15. A. Borawski, "Coatings in Industry Research Methods—A Short Review," *Coatings* 12 (2022): 1924.

16. A. B. Pursglove and B. G. Dale, "Developing a Quality Costing System: Key Features and Outcomes," *Omega* 23 (1995): 567–575.

17. S. Abdollahi Baghban, M. Ebrahimi, M. Khorasani, and S. Bagheri-Khoulenjani, "Tailoring A Variety of Self-Stratifying Patterns in A Light-Curable Coating on the Substrates With Different Surface Free Energies," *Progress in Organic Coatings* 171 (2022): 107023.

18. M. I. Baig, J. D. Willott, and W. M. de Vos, "Enhancing the Separation Performance of Aqueous Phase Separation-Based Membranes through Polyelectrolyte Multilayer Coatings and Interfacial Polymerization," *ACS Applied Polymer Materials* 3 (2021): 3560–3568.

19. J. E. Krzanowski, "Phase Formation and Phase Separation in Multiphase Thin Film Hard Coatings," *Surface and Coatings Technology* 188-189 (2004): 376–383.

20. V. Verkholantsev and M. Flavian, "Polymer Structure and Properties of Heterophase and Self-Stratifying Coatings," *Progress in Organic Coatings* 29 (1996): 239–246.

21. A. Abbasian, S. Ekbatani, and N. Bagherzadeh, "On The Stratification Mechanism of Self-Stratifying Epoxy–Acrylic Coatings," *Journal of Coatings Technology and Research* 18 (2021): 559–568.

22. H. Kuczyńska, E. Langer, E. Kamińska-Tarnawska, D. A. Kulikov, and E. A. Indeikin, "Study of Self-Stratifying Compositions," *Journal of Coatings Technology and Research* 6 (2009): 345–352.

23. S. J. Rinehart, G. Yuan, and M. D. Dadmun, "Elucidating the Kinetic and Thermodynamic Driving Forces in Polymer Blend Film Self-Stratification," *Macromolecules* 51 (2018): 7836–7844.

24. R. Evans, M. C. Stewart, and N. B. Wilding, "A Unified Description of Hydrophilic and Superhydrophobic Surfaces In Terms of The Wetting and Drying Transitions of Liquids," *Proceedings of the National Academy of Sciences* 116 (2019): 23901–23908.

25. B. R. Freedman, J. A. Cintron Cruz, P. Kwon, et al., "Instant Tough Adhesion of Polymer Networks," *Proceedings National Academy Sciences* 121 (2024): e2304643121.

26. N. Kargarfard, F. Simon, K. Schlenstedt, et al., "Self-Stratifying Powder Coatings Based on Eco-Friendly, Solvent-Free Epoxy/Silicone Technology for Simultaneous Corrosion and Weather Protection," *Progress in Organic Coatings* 161 (2021): 106443.

27. J. Baghdachi, H. Perez, and P. Talapatcharoenkit, "Chapter 6-Self-Stratifying Polymers and Coatings," in *Functional Polymer Coatings*, edited by L. Wu and J. Baghdachi, Wiley, Hoboken. ISBN 978-1-118-51070-4.

28. S. Zahedi and S. R. Ghaffarian, "A New Approach To Design of Anti-Corrosive Three Layers Self-Stratifying Coatings," *Transactions of the IMF* 99 (2021): 133–140.

29. H. He, T. Yang, Y. Liu, Y. Du, and F. Liang, "Self-Stratifying Coating with Robust and Durable Superhydrophobic Underlayer Constructed by Amphiphilic Janus Nanoparticles," *Chemistry of Materials* 35 (2023): 6083–6096.

30. L. Wang, L. Wang, J. Wu, et al., "Exploring the Mechanism of Self-Stratifying Coatings With Aggregation-Induced Emission," *Progress in Organic Coatings* 159 (2021): 106448.

31. W. Tang, Y. Su, Y. Huang, Y. Yu, H. Chen, and I. Chu, "Polymers Dynamics of The Nonfluoro, Nano-Brush Repelling Agent With Self-Stratifying Property in Water-Based Coatings," *Journal of Applied Polymer Science* 136 (2019): 48003.

32. Y. Yao, Z. Xu, B. Liu, M. Xiao, J. Yang, and W. Liu, "Multiple H-Bonding Chain Extender-Based Ultrastiff Thermoplastic Polyurethanes with Autonomous Self-Healability, Solvent-Free Adhesiveness, and Aie Fluorescence," *Advanced Functional Materials* 31 (2021): 2006944.

33. J. Zhou, H. Liu, Y. Sun, C. Wang, and K. Chen, "Self-Healing Titanium Dioxide Nanocapsules-Graphene/Multi-Branched Polyurethane Hybrid Flexible Film With Multifunctional Properties Toward Wearable Electronics," *Advanced Functional Materials* 31 (2021): 2011133.

34. M. Choi, Y. Kim, S. Park, et al., "Functionalized Polyurethane-Coated Fabric with High Breathability, Durability, Reusability, and Protection Ability," *Advanced Functional Materials* 31 (2021): 2101511.

35. H. R. Asemani and V. Mannari, "Ambient Temperature and Uv-Cured Hybrid Coatings from Acetoacetylated Non-Isocyanate Polyurethanes," *Journal of Coatings Technology and Research* 18 (2021): 469–488.

36. H. R. Asemani and V. Mannari, "Dual-Curable Coatings Obtained from Multi-Functional Non-Isocyanate Polyurethane Oligomers," *Journal of Coatings Technology and Research* 19 (2022): 1393–1407.

37. U. Sundararaj and C. W. Macosko, "Drop Breakup and Coalescence in Polymer Blends: The Effects of Concentration and Compatibilization," *Macromolecules* 28 (1995): 2647–2657.

38. D. G. Bae, R. K. Mandel, S. V. Dessiatoun, et al., "Embedded Two-Phase Cooling of High Heat Flux Electronics On Silicon Carbide (Sic) Using Thin-Film Evaporation and An Enhanced Delivery System (Feeds) Manifold-Microchannel Cooler," *16th IEEE Intersociety Conference on Thermal and Thermomechanical Phenomena in Electronic Systems (ITherm)* (2017): 466–472.

39. K. Zhang, L. Bai, H. Jin, G. Lin, G. Yao, and D. Wen, "A Comparative Study Of Pool Boiling Heat Transfer In Different Porous Artery Structures," *Applied Thermal Engineering* 202 (2022): 117759.

40. M. B. Yagci, S. Bolca, J. P. A. Heuts, W. Ming, and G. De With, "Self-Stratifying Antimicrobial Polyurethane Coatings," *Progress in Organic Coatings* 72 (2011): 305–314.

41. P. Rocas, Y. Fernández, S. Schwartz, I. Abasolo, J. Rocas, and F. Albericio, "Multifunctionalized Polyurethane–Polyurea Nanoparticles: Hydrophobically Driven Self-Stratification At The O/W Interface Modulates Encapsulation Stability," *Journal of Materials Chemistry B* 3 (2015): 7604–7613.

42. X. Yang, Z. Su, D. Wu, S. L. Hsu, and H. D. Stidham, "Raman Analysis of a Conformational Distribution of Poly(ethylene oxide) and Its Model Compound in the Liquid State," *Macromolecules* 30 (1997): 3796–3802.

43. I. Blakey and G. A. George, "Raman Spectral Mapping of Photo-Oxidised Polypropylene," *Polymer Degradation and Stability* 70 (2000): 269–275.

44. M. Gorbounov, P. Halloran, and S. Masoudi Soltani, "Hydrophobic and Hydrophilic Functional Groups and Their Impact on Physical Adsorption Of Co2 In Presence Of H2o: A Critical Review." *Journal of CO2 Utilization* 86 (2024): 102908.

45. S. Pérez-Conesa, P. M. Piaggi, and M. Parrinello, "A Local Fingerprint for Hydrophobicity And Hydrophilicity: from Methane to Peptides," *Journal of Chemical Physics* 150 (2019): 204103.

46. M. Y. Bashouti, Y. Paska, S. R. Puniredd, T. Stelzner, S. Christiansen, and H. Haick, "Silicon Nanowires Terminated With Methyl Functionalities Exhibit Stronger Si–C Bonds Than Equivalent 2d Surfaces," *Physical Chemistry Chemical Physics* 11 (2009): 3845–3848.

47. N. K. Howell, G. Arteaga, S. Nakai, and E. C. Y. Li-Chan, "Raman Spectral Analysis in the C−H Stretching Region of Proteins and Amino Acids for Investigation of Hydrophobic Interactions," *Journal of Agricultural and Food Chemistry* 47 (1999): 924–933.

48. I. Fratoddi, I. Venditti, C. Battocchio, et al., "Highly Hydrophilic Gold Nanoparticles as Carrier for Anticancer Copper(I) Complexes: Loading and Release Studies for Biomedical Applications," *Nanomaterials* 9 (2019): 772.

49. T.-Y. Lo, A. Dehghan, P. Georgopanos, A. Avgeropoulos, A.-C. Shi, and R.-M. Ho, "Orienting Block Copolymer Thin Films via Entropy," *Macromolecules* 49 (2016): 624–633.

50. M. Sikka, N. Singh, A. Karim, F. S. Bates, S. K. Satija, and C. F. Majkrzak, "Entropy-Driven Surface Segregation In Block Copolymer Melts," *Physical Review Letters* 70 (1993): 307.

51. M. W. Matsen, "Architectural Effect on the Surface Tension of an ABA Triblock Copolymer Melt," *Macromolecules* 43 (2010): 1671–1674.

52. V. Khanna, E. W. Cochran, A. Hexemer, et al., "Effect of Chain Architecture and Surface Energies on the Ordering Behavior of Lamellar and Cylinder Forming Block Copolymers," *Macromolecules* 39 (2006): 9346–9356.

53. D. T. Wu, G. H. Fredrickson, J. Carton, A. Ajdari, and L. Leibler, "Distribution of Chain Ends At The Surface of A Polymer Melt: Compensation Effects and Surface Tension," *Journal of Polymer Science Part B: Polymer Physics* 33 (1995): 2373–2389.

54. M. W. Matsen and P. Mahmoudi, "Segregation of Chain Ends to The Surface of A Polymer Melt," *The European Physical Journal E* 37 (2014): 78.

55. D. S. Kim, J. Kim, and W. B. Woo, "Reaction Kinetics and Characteristics of Polyurethane/Clay Nanocomposites," *Journal of Applied Polymer Science* 96 (2005): 1641–1647.

56. A. Olejnik, K. Gosz, and Ł. Piszczyk, "Kinetics of Cross-Linking Processes of Fast-Curing Polyurethane System," *Thermochimica Acta* 683 (2020): 178435.

57. V. S. Sivasankar, S. A. Etha, D. R. Hines, and S. Das, "Coalescence of Microscopic Polymeric Drops: Effect of Drop Impact Velocities," *Langmuir* 37 (2021): 13512–13526.

58. L. Shen, G. D. Gorbea, E. Danielson, S. Cui, C. J. Ellison, and F. S. Bates, "Threading-the-Needle: Compatibilization of HDPE/i PP blends with butadiene-derived polyolefin block copolymers," *Proceedings of the National Academy of Sciences* 120 (2023): 2301352120.

59. I. Fortelný and J. Kovář, "Theory of Coalescence In Immiscible Polymer Blends," *Polymer Composites* 9 (1988): 119–124.

Supporting Information

Additional supporting information can be found online in the Supporting Information section.

Supporting File: mame70145-sup-0001-SuppMat.pdf.